

# Universal manuscript template for Optica Publishing Group journals

## 1. Abstract

2 Lorem ipsum ~100 words

## 3 2. Introduction

4 IR spectroscopy has seen significant interest and application in bio-imaging because it provides a  
5 chemical fingerprint of underlying samples in a label-free way [1]. However, although the most  
6 relevant chemical information can be gathered in the mid-infrared ( $\sim 3 - 12 \mu\text{m}$ ), slow signal  
7 acquisition is often a limiting factor, whose trade-off can keep it from competing with label-based  
8 fluorescence microscopy.

9 Fig. 1 attempts to visualize the significant developments that have been made in mid-infrared  
10 hyperspectral imaging over roughly the last two decades. Experiments are mapped onto the  
11 two important metrics of spectra acquisition speed, which captures the rate at which spectra  
12 are gathered, and optical bandwidth, which captures the breadth of chemical content that can  
13 be observed. The two variables are plotted against each other, since a significant difficulty lies  
14 in achieving both metrics simultaneously. For a better one to one comparison, the acquisition  
15 speeds listed for experiments that use focal plane arrays have been normalized to that of an  
16 analogous point scanning experiment.  
17

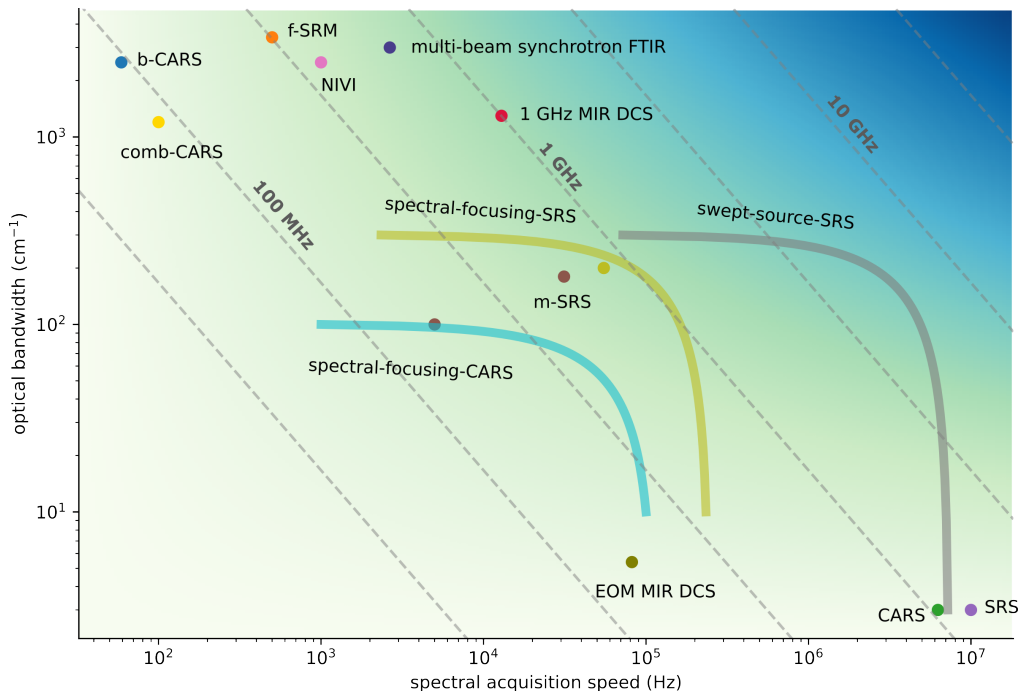


Fig. 1. Performance map of mid-infrared hyperspectral imaging. Broadband CARS (b-CARS) [2], femtosecond Stimulated Raman Microscopy (f-SRM) [3], in-vivo video rate CARS [4], in-vivo video rate SRS [5], multiplexed SRS (m-SRS) [6, 7], nonlinear interferometric vibrational imaging (NIVI) [8], swept-source SRS [9], spectral-focusing SRS [10], spectral-focusing CARS [11], spectral-focusing SRS [12], comb-CARS [13], multi-beam synchrotron FTIR [14], electro-optic modulator comb MIR DCS [15]

19 A few of the most notable experiments have utilized coherent Raman spectro-imaging, where  
 20 in-vivo video-rate speeds have been demonstrated in the mid-infrared [4, 5]. Whereas initial  
 21 demonstrations were over a narrow bandwidth ( $\sim 3 \text{ cm}^{-1}$ ), broad bandwidths at high acquisition  
 22 speeds have been demonstrated using rapidly rotating polygonal mirror scanners [12, 16]. However,  
 23 the stated metrics are only possible with the strong Raman absorption cross-sections around  
 24  $2900 \text{ cm}^{-1}$ , which precludes Raman spectroscopy-based platforms from achieving the same  
 25 performance in the fingerprint region at longer wavelengths.

26 Conversely, Fourier transform spectroscopy (FTS) and quantum cascade laser (QCL) based  
 27 imaging are attractive due to their broad applicability across the mid to long wavelength infrared.  
 28 The high absorption cross-sections can also alleviate the need for operation at powers close to  
 29 sample-damage thresholds, a concern that is applicable to biological samples. In this category,  
 30 FTS spectrometers coupled to broadband and bright sources such as synchrotron facilities have  
 31 set the state of the art for the combination of spectral bandwidth and speed [14]. The coupling of  
 32 broadband synchrotron light into a microscope requires the active stabilization of a beam bundle.  
 33 However, a widely accessible imaging method would benefit from having a simple and table  
 34 top setup. QCL lasers are attractive due to their direct emission in the mid-infrared and small  
 35 footprint, although their performance is best leveraged in narrowband applications. Tunable QCL  
 36 packages consisting of multiple QCL chips combined into one device [17] can nominally reach  
 37 broad spectral coverage, but struggle to reach noise figures comparable to platforms based on  
 38 mode-locked lasers.

More recently, dual-comb spectroscopy (DCS) in the frequency comb community has become  
 a popular platform, due to its improved stability and speed when compared to classical FTS [18].  
 In this modality, the interference of two frequency combs maps a Nyquist band from the optical  
 domain down into the RF. One of the most important considerations in DCS is the direct trade-off  
 between the frequency resolution/repetition rate  $f_r$  and the size of the optical Nyquist window  
 $\Delta\nu$ :

$$\Delta\nu = \frac{f_r^2}{2\Delta f_r} \quad (1)$$

39 where  $\Delta f_r$  is the interferogram acquisition rate equal to the difference of the two laser rep-rates.  
 40 The diagonal dashed lines in Fig. 1., show the  $f_r^2/2$  trade-off between resolvable bandwidth and  
 41 acquisition speed in DCS for different  $f_r$ . Evidently, when broad absorption features allow for  
 42 coarse resolution, the highest rep-rates are desired. However, in order to reach sufficient power  
 43 per comb tooth, in practice the pulse energy required for nonlinear frequency down-conversion  
 44 from the near-infrared sets an upper limit on the obtainable rep-rate. In this work, we utilize a  
 45 set of recently developed 1-GHz mid-infrared frequency combs [19] to integrate a dual-comb  
 46 spectrometer with a confocal microscope. We capitalize on the high repetition rate by fully filling  
 47 the third Nyquist band ( $2595 \text{ cm}^{-1}$ – $3890 \text{ cm}^{-1}$  at  $\Delta f_r = 12.86 \text{ kHz}$ ). The system is among the  
 48 fastest performers in the class of spectrometers covering over  $1000 \text{ cm}^{-1}$  with high spectral  
 49 resolution in the mid-infrared.

50 However, pointing to the dashed line in the upper right corner of Fig. 1, in order to achieve the  
 51 ultimate goal of label-free broadband video-rate imaging, we note that the ideal DCS platform  
 52 would operate with repetition rates of 10 GHz or higher. Such systems would likely require either  
 53 high-power amplifiers or a nanophotonic design capable of generating equivalent bandwidths in  
 54 the mid-infrared with pump pulse energies around 100 pJ.

### 55 3. Experiment

56 With long-term stability in mind, a single-branch intra-pulse difference frequency generation  
 57 (DFG) design is used to generate light in the mid-infrared [19]. Shown in Fig. 2, to compensate  
 58 for the low conversion efficiency of the single-branch design, octave spanning few cycle NIR

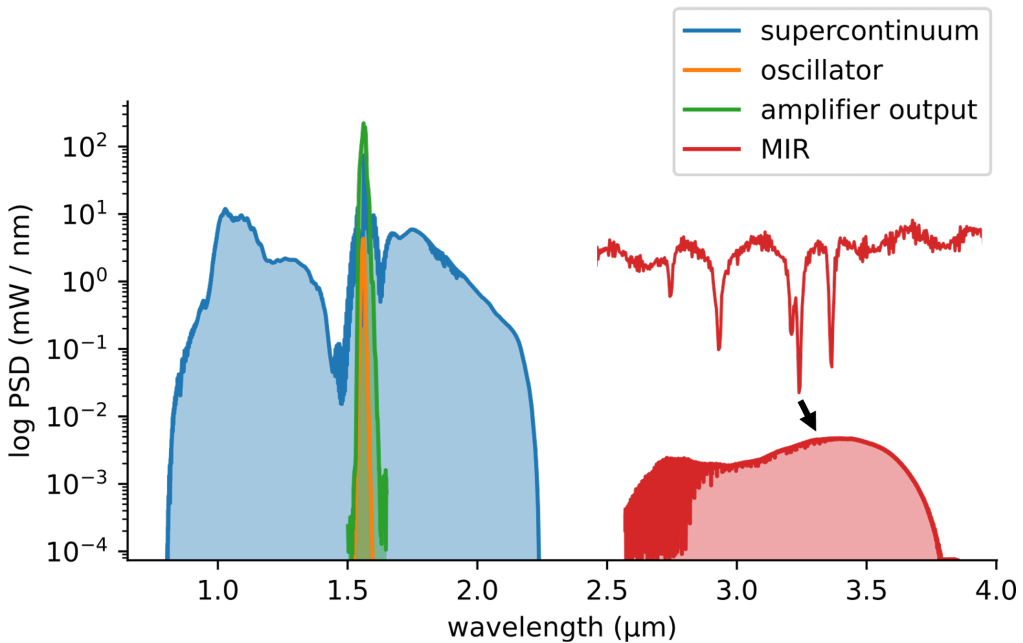


Fig. 2. 1 GHz MIR Frequency Comb. The spectral evolution through successive stages of the system: oscillator → chirped-pulse amplifier → few-cycle supercontinuum generation → MIR frequency down conversion. The inset shows a zoom in of waterlines that are resolved when using the full 1 GHz frequency resolution.

59 pulses generated via soliton self-compression in anomalous dispersion highly nonlinear fiber are  
 60 used to drive the nonlinear frequency down conversion to the mid-infrared. Although coverage  
 61 of the 6-12  $\mu\text{m}$  wavelength region can be achieved for one laser system, due to the lack of  
 62 nonlinear crystals in this work more widely available lithium niobate is used to cover the 3 - 5  
 63  $\mu\text{m}$  wavelength window.

64 Two 1-GHz mid-infrared frequency combs are generated and coupled into  $\text{InF}_3$  single-mode  
 65 fiber for delivery to the experiment. The output beam is collimated with a two inch off-axis  
 66 parabolic mirror, and a reflective confocal microscope with 0.58 NA is used to image the beam  
 67 onto a glass slide ( $\sim 3.8 \mu\text{m}$  pixel size). A set of linear translation stages are used to raster scan  
 68 the sample. The data is acquired via trigger, with the trigger spacing and scan speed set by the  
 69 desired spatial sampling interval. The scan speed is limited only by the interferogram acquisition  
 70 time, which is fundamentally set by the repetition rate of the laser. The transmitted signal is  
 71 focused onto a high-speed MCT detector, whose AC coupled port is digitized at 1 GS/s using an  
 72 FPGA. The data is streamed concurrently from the card memory into PC RAM for real-time  
 73 analysis, and such that the card-memory does not limit the data volume. Owing to the fairly high  
 74 500 MHz Nyquist frequency, and the placement of all fiber amplifiers in loop for the phase-locks  
 75 of the two frequency combs, over one thousand interferograms can be directly averaged before  
 76 phase correction needs to be employed.

#### 77 4. Results

78 As a demonstration, hyperspectral images are taken of a USAF resolution target composed of  
 79 SU-8 photoresist patterned onto a 500  $\mu\text{m}$  thick Silicon wafer. Five hundred spectra (39 ms) are  
 80 averaged at each pixel and apodized to 100 GHz ( $3.3 \text{ cm}^{-1}$ ). Point spectra shown in Fig. 4.(b).  
 81 are taken at each pixel to generate the hypercube. The images are generated by integrating a

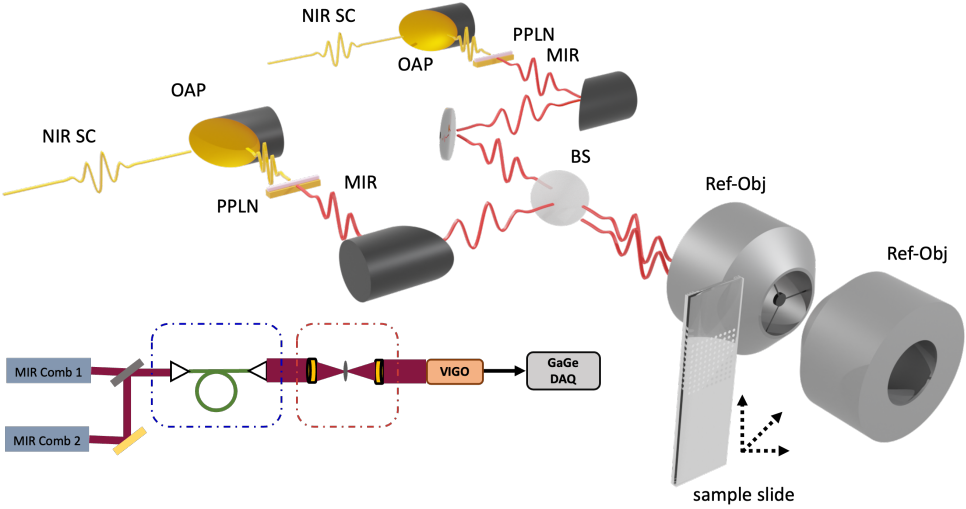


Fig. 3. Experimental Setup. Two mid-infrared frequency combs generated through intra-pulse difference frequency generation are passed collinearly through a confocal microscope. Hyperspectral images are collected by raster scanning the sample slide. The transmitted signal is collected and digitized in a high-speed MCT mid-infrared detector and FPGA.

82 ~63 cm<sup>-1</sup> window around the peak absorption at ~2930 cm<sup>-1</sup>.

83 For a biologically relevant sample, we image a cross-section of ovarian cancer tissue (... add  
 84 info), where the paraffin wax was removed prior to dual-comb imaging. To bench mark  
 85 performance, we compare the results of DCS point scanning microscopy to hyperspectral data  
 86 taken with a commercial FTIR microscope using a focal plane array. Five hundred spectra are  
 87 again averaged at each pixel and apodized to 3.3 cm<sup>-1</sup>. Point spectra such as the one shown  
 88 by the orange curve in Fig. 5.(b). are collected at each pixel, with the two C-H anti-symmetric  
 89 stretch bands visible at 2850 and 2920 cm<sup>-1</sup>. A DCS spectrum taken with a two second averaging  
 90 time (25,700 averages) is shown by the green curve, and a comparison spectrum taken using  
 91 a commercial FTIR with 7.61 cm<sup>-1</sup> frequency resolution (... add info) is shown by the red  
 92 curve. Apart from a broadening of the peak, good qualitative agreement is observed between  
 93 the DCS and FTIR spectra. The FTIR image was taken prior to the removal of paraffin wax,  
 94 which accounts for the peak broadening when compared to the spectra taken using DCS. The  
 95 images are generated by taking a slice through the hypercube at the peak of the 2920 cm<sup>-1</sup> band.  
 96 A coarse image shown in Fig. 5(c). with 5 μm sampling is taken of the entire core. A zoom-in  
 97 of the sample is shown in Fig. 5(a.), taken at 1.2 μm sampling, which is approximately the  
 98 Nyquist sampling limit of the microscope. The image shows generally good agreement with the  
 99 corresponding image in Fig. 5(d). taken using FTIR. We note that the dim vertical lines in the  
 100 DCS image are attributed to the limited ~1.5 μm repeatability of the translation stages (Thorlabs  
 101 Z825B).

## 102 5. DCS Imaging Speed

Regardless of the imaging method, the final determination of imaging speed is given by the time  
 needed to reach sufficient SNR at each pixel. Specifically for DCS microscopy, the target SNR  
 and frequency resolution sets the pixel dwell time. In DCS, the absorbance noise  $\sigma$  scales with

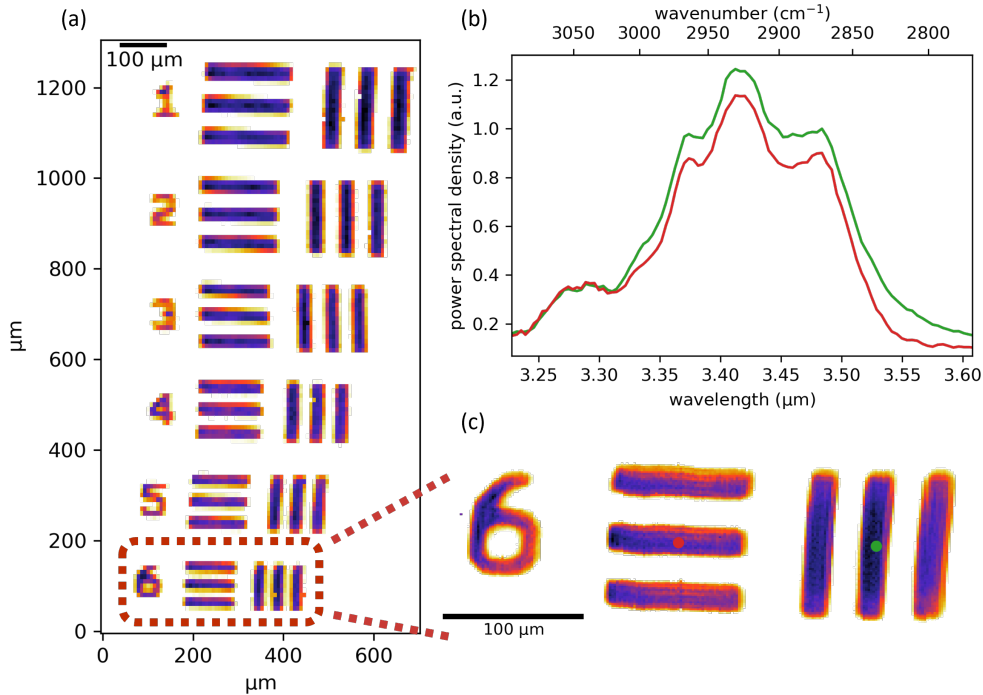


Fig. 4. Caption

the frequency resolution and number of averaged spectra  $N_{avg}$  according to [20]:

$$\sigma \propto \frac{N}{\sqrt{N_{avg}}} \quad (2)$$

where  $N$  is the number of frequency bins. This scaling rule is shown in Fig. 6.(c-d)., where it is observed to match the experimentally measured absorbance noise. The two-variable map in Fig. 6.(d). should apply more generally to any DCS point scanning microscopy, but with the time axis scaled accordingly to the repetition rate.

Shown in Fig. 6.(a)., a baseline for 1 GHz DCS is that a  $1000 \text{ cm}^{-1}$  Nyquist window can be covered with  $\sim 17$  kHz spectra acquisition speed, which is a two order magnitude improvement over well established 100 MHz mid-infrared dual-comb systems. In Fig. 6.(b)., a single-shot spectrum ( $77 \mu\text{s}$ ) at 1-GHz has low signal to noise, but can be averaged to high SNR in two seconds ( $>25,000$  spectra). However, a high SNR can be achieved in  $\sim 39$  ms at 500 averages if the interferograms are apodized to 100 GHz ( $\sim 3.33 \text{ cm}^{-1}$ ). The SNR as a function of averaging time and frequency resolution is shown in Fig. 6.(c-d).; the absorbance noise always averages down according to  $1/\sqrt{N_{avg}}$ , but with coarser resolution resulting in a directly proportional overall noise reduction.

## References

1. M. J. Baker, J. Trevisan, P. Bassan, R. Bhargava, H. J. Butler, K. M. Dorling, P. R. Fielden, S. W. Fogarty, N. J. Fullwood, K. A. Heys, C. Hughes, P. Lasch, P. L. Martin-Hirsch, B. Obinaju, G. D. Sockalingum, J. Sulé-Suso, R. J. Strong, M. J. Walsh, B. R. Wood, P. Gardner, and F. L. Martin, "Using Fourier transform IR spectroscopy to analyze biological materials," *Nat. Protoc.* **9**, 1771–1791 (2014).
2. T. W. Kee and M. T. Cicerone, "Simple approach to one-laser, broadband coherent anti-Stokes Raman scattering microscopy," *Opt. Lett.* **29**, 2701 (2004).

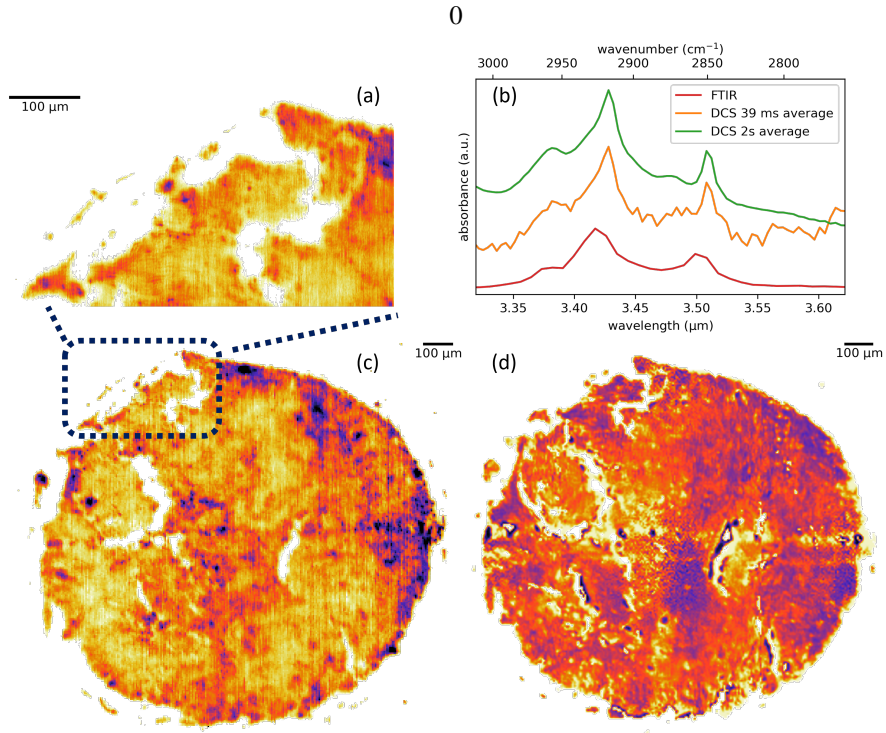


Fig. 5. Caption

- 123 3. E. Ploetz, S. Laimgruber, S. Berner, W. Zinth, and P. Gilch, "Femtosecond stimulated Raman microscopy," *Appl. Phys. B* **87**, 389–393 (2007).
- 124 4. C. L. Evans, E. O. Potma, M. Puoris'haag, D. Côté, C. P. Lin, and X. S. Xie, "Chemical imaging of tissue *in vivo* with video-rate coherent anti-Stokes Raman scattering microscopy," *Proc. National Acad. Sci.* **102**, 16807–16812 (2005).
- 125 5. B. G. Saar, C. W. Freudiger, J. Reichman, C. M. Stanley, G. R. Holtom, and X. S. Xie, "Video-Rate Molecular Imaging In Vivo with Stimulated Raman Scattering," *Science* **330**, 1368–1370 (2010).
- 126 6. D. Fu, F.-K. Lu, X. Zhang, C. Freudiger, D. R. Pernik, G. Holtom, and X. S. Xie, "Quantitative Chemical Imaging with Multiplex Stimulated Raman Scattering Microscopy," *J. Am. Chem. Soc.* **134**, 3623–3626 (2012).
- 127 7. C.-S. Liao, M. N. Slipchenko, P. Wang, J. Li, S.-Y. Lee, R. A. Oglesbee, and J.-X. Cheng, "Microsecond scale vibrational spectroscopic imaging by multiplex stimulated Raman scattering microscopy," *Light. Sci. & Appl.* **4**, e265–e265 (2015).
- 128 8. P. D. Chowdary, Z. Jiang, E. J. Chaney, W. A. Benalcazar, D. L. Marks, M. Gruebele, and S. A. Boppart, "Molecular Histopathology by Spectrally Reconstructed Nonlinear Interferometric Vibrational Imaging," *Cancer Res.* **70**, 9562–9569 (2010).
- 129 9. Y. Ozeki, W. Umemura, Y. Otsuka, S. Satoh, H. Hashimoto, K. Sumimura, N. Nishizawa, K. Fukui, and K. Itoh, "High-speed molecular spectral imaging of tissue with stimulated Raman scattering," *Nat. Photonics* **6**, 845–851 (2012).
- 130 10. D. Fu, G. Holtom, C. Freudiger, X. Zhang, and X. S. Xie, "Hyperspectral Imaging with Stimulated Raman Scattering by Chirped Femtosecond Lasers," *The J. Phys. Chem. B* **117**, 4634–4640 (2013).
- 131 11. C. Di Napoli, I. Pope, F. Masia, P. Watson, W. Langbein, and P. Borri, "Hyperspectral and differential CARS microscopy for quantitative chemical imaging in human adipocytes," *Biomed. Opt. Express* **5**, 1378 (2014).
- 132 12. H. Lin, H. J. Lee, N. Tague, J.-B. Lugagne, C. Zong, F. Deng, J. Shin, L. Tian, W. Wong, M. J. Dunlop, and J.-X. Cheng, "Microsecond fingerprint stimulated Raman spectroscopic imaging by ultrafast tuning and spatial-spectral learning," *Nat. Commun.* **12**, 3052 (2021).
- 133 13. T. Ideguchi, S. Holzner, B. Bernhardt, G. Guelachvili, N. Picqué, and T. W. Hänsch, "Coherent Raman spectro-imaging with laser frequency combs," *Nature* **502**, 355–358 (2013).
- 134 14. M. J. Nasse, M. J. Walsh, E. C. Mattson, R. Reininger, A. Kajdacsy-Balla, V. Macias, R. Bhargava, and C. J. Hirschmugl, "High-resolution Fourier-transform infrared chemical imaging with multiple synchrotron beams," *Nat. Methods* **8**, 413–416 (2011).

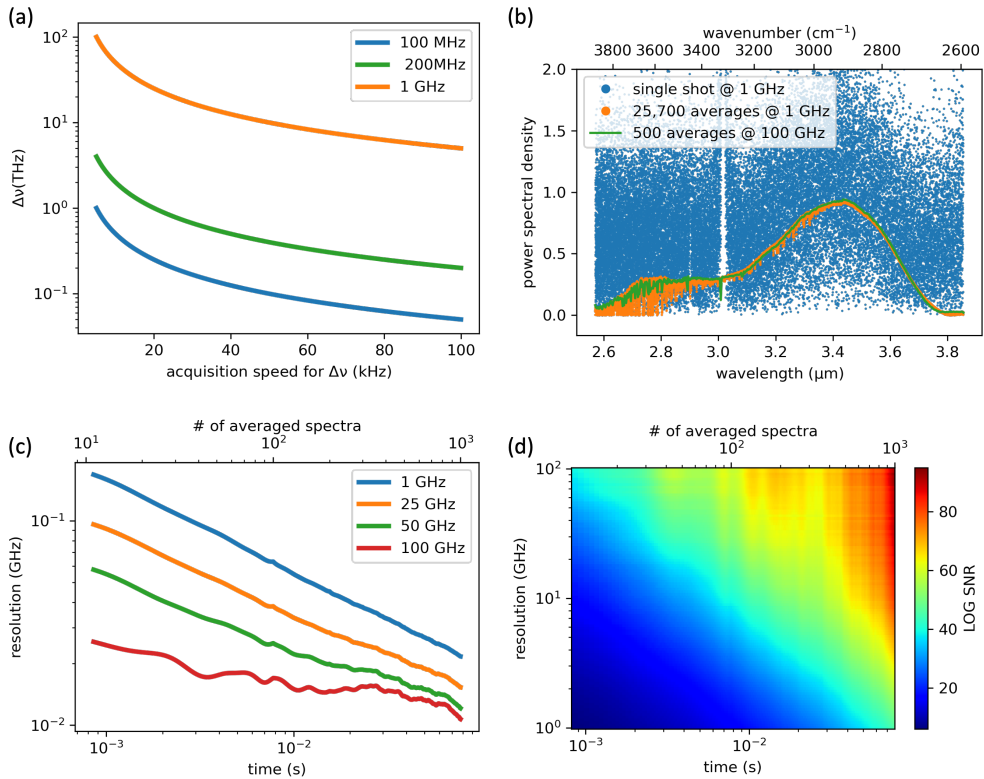


Fig. 6. Summary of DCS Imaging Speed. (a) The size of the optical Nyquist window plotted against acquisition speed ( $\Delta f_r$ ) for different repetition rates. (b) DCS spectrum taken at different averaging times and frequency resolution/apodization windows. (c) The spectra's SNR follow the scaling of Eq.2, with an example of the 2D parameter space (d) mapped out for the 1-GHz system.

- 152 15. F. Ullah Khan, G. Guarnizo, and P. Martín-Mateos, "Direct hyperspectral dual-comb gas imaging in the mid-infrared,"  
153 Opt. Lett. **45**, 5335 (2020).
- 154 16. M. Tamamitsu, Y. Sakaki, T. Nakamura, G. K. Podagatlapalli, T. Ideguchi, and K. Goda, "Ultrafast broadband  
155 Fourier-transform CARS spectroscopy at 50,000 spectra/s enabled by a scanning Fourier-domain delay line," Vib.  
156 Spectrosc. **91**, 163–169 (2017).
- 157 17. K. Yeh, S. Kenkel, J.-N. Liu, and R. Bhargava, "Fast Infrared Chemical Imaging with a Quantum Cascade Laser,"  
158 Anal. Chem. **87**, 485–493 (2015).
- 159 18. I. Coddington, N. Newbury, and W. Swann, "Dual-comb spectroscopy," Optica **3**, 414 (2016).
- 160 19. N. Hoghooghi, S. Xing, P. Chang, D. Lesko, A. Lind, G. Rieker, and S. Diddams, "Broadband 1-GHz mid-infrared  
161 frequency comb," Light. Sci. & Appl. **11**, 264 (2022).
- 162 20. N. R. Newbury, I. Coddington, and W. Swann, "Sensitivity of coherent dual-comb spectroscopy," Opt. Express **18**,  
163 7929 (2010).